

## PLANCK CLUSTER PAPER

SB<sup>1</sup>, JPH<sup>1</sup>, FM, PD<sup>1</sup>

Draft Version May 21, 2018

### ABSTRACT

We propose to continue our program of optical imaging to unveil all of the most massive clusters in the observable Universe. We start from the all-sky *Planck* Sunyaev-Zeldovich (SZ) catalogs, which contain several hundred high significance (signal-to-noise ratio, SNR > 5) unconfirmed cluster candidates. Since SZ selection favors high mass clusters and the *Planck* confirmation process favored low redshift systems, the highest significance unconfirmed candidates are, therefore, likely massive clusters ( $M_{500} > 5 \times 10^{14} M_{\odot}$ ) at relatively high redshift ( $z > 0.5$ ). Our proposed observations, using MOSAIC-3 on Mayall, are designed to confirm the presence of a brightest cluster galaxy (to  $z \sim 1$ ) and red sequence of accompanying cluster members (to  $z \sim 0.7$ ). Preliminary results from our observations over the past two years have validated our approach by the detection of optical clusters in a number of *Planck* candidates, including the discovery of rich systems at  $z = 0.553$  and  $z = 0.830$  that rival the most massive clusters known. The proposed observations represent the first step required to provide a complete all-sky census throughout the observable Universe of the most massive, high redshift clusters. Their expected high redshift and high mass make the unconfirmed *Planck* clusters, arguably, the most important available sample for probing deviations from  $\Lambda$ CDM and defining the high-mass end of the cluster mass function.

### 1. INTRODUCTION

this section has not been edited and is just a bunch of stuff copy and pasted. I did update some of the references.

Massive clusters of galaxies are the extraordinary objects which hold important clues to the evolution of structure in the universe. The widely accepted  $\Lambda$ CDM model of cosmology makes specific predictions about the mass distribution of galaxy clusters in the universe. The number of galaxy clusters, especially at high redshifts, can help constrain structure formation models (e.g., Mortonson et al. 2011; Harrison & Coles 2012; Harrison & Hotchkiss 2012; Waizmann et al. 2012; Zitrin et al. 2009). Galaxy clusters also harbor a significant fraction of the visible baryons in the Universe, in the form of a hot intracluster medium that leaves an imprint on the Cosmic Microwave Background (CMB) through the Sunyaev-Zel'dovich effect (SZ; Sunyaev & Zeldovich 1972 effect).

Using the SZ effect to discover clusters of galaxies has the distinct advantage that the surface brightness of the SZ effect does not dim with increasing redshift. This allows homogeneous samples of massive clusters to be detected out to arbitrary distances. Ground based, large area-sky surveys such as those with the Atacama Cosmology Telescope (ACT; Swetz et al. 2011) and the South Pole Telescope (SPT; Carlstrom et al. 2011) have produced catalogs of hundreds of massive clusters below  $z \sim 1.4$  (e.g., Hasselfield et al. 2013; Reichardt et al. 2013). Now, *Planck* (Tauber et al. 2010; Planck Collaboration et al. 2011) has released an all-sky SZ sample (PSZ; Planck Collaboration et al. 2014, 2015) that contains 861 confirmed clusters (of which most [683] were known previously) and another 366 unconfirmed cluster candidates.

Clusters were initially confirmed by cross correlating

with previous catalogs (see Section 4; Planck Collaboration et al. 2014). More recently, dedicated follow up of still-unconfirmed clusters has begun in earnest (e.g., Liu et al. 2015; Planck Collaboration et al. 2015, 2016; Burenin 2017; Barrena et al. 2018; Amodeo et al. 2018; Strebyanska et al. 2018).

This paper is organized as follows: sections 2 through 4 describe the design, observations, data reduction and calibration, and creation of derived data products. In Section 5, we present the main results of our observations, and discuss the results in Section 6. In Section 7, we summarize the key results and conclude.

Unless otherwise noted, throughout this paper, we use a concordance cosmological model ( $\Omega_{\Lambda} = 0.7$ ,  $\Omega_m = 0.3$ , and  $H_0 = 70 \text{ km s}^{-1}\text{Mpc}^{-1}$ ), assume a Chabrier initial mass function (Chabrier 2003), and use AB magnitudes (Oke 1974).

### 2. DESIGN

Among the recently released, second, all-sky PSZ catalog<sup>2</sup> (hereafter PSZ2; Planck Collaboration et al. 2015) there are 450 unconfirmed SZ detections with S/N > 4.5. The vast majority of these must lie at high-z because the *Planck* confirmation process (Planck Collaboration et al. 2014) mostly relied on existing catalogs with a preference for low-z clusters. Furthermore, the confirmed sample has a small fraction (3%) of  $z > 0.6$  clusters compared to that expected ( $\sim 20\%$ ) based on the theoretical halo mass function (e.g., Jenkins et al. 2001; Tinker et al. 2008). If other clusters like “El Gordo” exist, they are hiding as high-significance candidates within the objects in this catalog. The design of the observations is to use optical imaging to confirm the SZ detections as real clusters and provide photometric redshifts using the multi-color information.

<sup>1</sup> Rutgers;boada@physics.rutgers.edu

<sup>2</sup> [http://szcluster-db.ias.u-psud.fr/sitools/client-user/SZCLUSTER\\_DA](http://szcluster-db.ias.u-psud.fr/sitools/client-user/SZCLUSTER_DA)

We design the observations based on the previous success with the ACT cluster confirmation process using 4-m class telescopes. Our strategy is to use the Kitt Peak National Observatory (KPNO) Mayall-4m telescope imaging as the first and fundamental step to confirm the highest significance detections in the PSZ2 catalog that are visible across the entire northern sky. Following closely the procedure used for ACT follow-up [citation?](#), targets are prioritized by SZ signal-to-noise (S/N). We choose to initially report on targets with PSZ2 S/N > 5 as the statistical reliability of PSZ2 cluster candidates is quite high: according to the *Planck* team  $\sim 90\%$  of candidates at S/N > 5 turn out to be “real” clusters ([citation? maybe show the figure from the proposal](#)).

Optical imaging will be sufficient to confirm nearly all of the candidates, but for the highest redshift ones, NIR data will be necessary. Again following the procedure for ACT cluster follow-up: those candidates with some evidence for a high-z brightest cluster galaxy (BCG; [note that we can detect BCGs to  \$z \sim 1.5\$](#) ) will be targeted with NIR observations to confirm the presence of a BCG and detect the red sequence of cluster members. Observational priority again is given to higher S/N candidates.

### 2.1. Observations

All observations were conducted with the KPNO Mayall telescope. The optical observations were made with the MOSAIC camera mounted at the prime focus. Two detector packages were used for the observations. The earlier MOSAIC1.1 instrument consisted of eight  $2048 \times 4096$  SiTe CCDs, arranged  $2 \times 4$ , separated by a  $\sim 50$  pixels gap with a pixel scale of  $0''.26$  pixel $^{-1}$ . MOSAIC1.1 was replaced with Mosaic3, in [year?](#), and consists of four new  $4k \times 4k$ , 15 micron pixel, 500-micron thick LBNL deep-depletion CCDs. Because the only change from MOSAIC1.1 to MOSAIC3 are the CCDs and controllers both versions have a  $36' \times 36'$  field-of-view.

[need to talk about the dithering](#)

The optical observing strategy consists of targeted *griz* observations of individual candidates with exposure times of 350 s, 350 s, 1100 s and 1100 s (assuming dark conditions) to provide  $5\sigma$  detections limits of  $g = ??$ ,  $r = 24.5$ ,  $i = 24.5$ ,  $z = 24.2$  ensuring the unambiguous detection of the faint (i.e.,  $0.4L\star$ ) galaxies in the red cluster sequence up to  $z \sim 1.0$  ([citation?](#)) and of brightest cluster galaxies (BCGs) to higher redshifts. The choice of filters in our program is driven by the need to segregate early-type galaxies in the cluster through their colors (or photometric redshifts) by sampling blue-ward and red-ward of the  $4000\text{\AA}$  break. [Our depths are quite a bit different than the designed depths. Should we mention that here, or wait till later on when we are discussing how we actually did?](#)

A summary of our observations is given in Table ??.

## 3. DATA REDUCTION AND CALIBRATION

Standard image reductions including subtraction of dark frames, flat fielding, sky-subtraction, and bad pixel masking was performed by the NOAO virtual observatory using the MOSAIC (Valdes & Swaters 2007) science pipelines. The resultant FITS files consist of fully reduced images with either all single exposure CCDs mosaicked into a single image extension (as in the case of

Mosaic1.1) or as a multi-extension FITS file with each single exposure CCD occupying a separate extension.

We then mosaic each separate exposure into a master mosaic as described in the following section.

### 3.1. Mosaicking

Combined mosaics are created with SWARP (Bertin et al. 2002). We create three distinct types of mosaics. The individual dither frames are stacked and then median combined to produce the final completed science mosaic. A “detection” is created by combining select science mosaics into a chi<sub>2</sub> image using either the *i*- and *z*-band when both are available and of sufficient quality. Finally we create a set of mosaics use to produce the three color image used for cluster finding. We median combine the *griz* science mosaics into a “blue” (*g*-band), “green” (*r*-band), and “red” (*iz*-band) mosaic. All final mosaics have a pixelscale of  $0''.25/\text{pix}$ . The final exposure time is calculated as the median exposure time of the combined images, and similarly the final airmass is median of the individual air masses. [need to talk about the weight images](#)

Finally, a smaller-sized ( $\sim 20'$  on a side) image is cropped from the full science mosaics. This small image serves as the actual science frame. The smaller size significantly decreases the number of sources recovered which reduces the time required to produce derived quantities (photometric redshifts, etc.).

The full parameter file used while creating the mosaics is given in Appendix ??.

### 3.2. Astrometric Calibration

Each of the final science mosaics produced in the previous section are first astrometrically aligned with *Gaia* (Gaia Collaboration et al. 2016a) Data Release 1 (Gaia Collaboration et al. 2016b) using SCAMP (Bertin 2006) as a part of PHOTOMETRYPipeline<sup>3</sup> (PP; Mommert & M. 2017).

Sources are extracted from the mosaics with a signal-to-noise ratio (SNR) of at least ten and with a minimum area of at least 12 pixels. The extracted sources are then matched to the *Gaia* data and a new astrometric solution is calculated. Because the initial astrometric solution from the VO is quite accurate, the resultant corrections are much less than  $1''$ .

### 3.3. Photometric Calibration

After the mosaics have been astrometrically aligned, we use PP to produce a photometric solution. PP calculates a photometric zero-point in each of our observed bands by comparing field stars located throughout the mosaic to known photometry from large-area sky surveys. Because our sources are spread across the entire northern sky, and because we prefer to minimize the number of differences between photometric solutions we are limited to two optical surveys. For the optical data, we first seek photometric data from the *Sloan Digital Sky Survey* (SDSS; York et al. 2000) Data Release 13 (Alam et al. 2015) [get a new citation for dr13 this is for dr12](#). When our target does not lie within the SDSS footprint we utilize the Panoramic Survey Telescope and Rapid

<sup>3</sup> <https://github.com/mommermi/photometrystreamline>

Response System (Pan-STARRS; Chambers et al. 2016) Data Release 1 (hereafter PS1; Flewelling et al. 2016). Both surveys provide accurate *griz* magnitudes and large on-line queriable databases for rapid automated calibration.

Sources are extracted from the combined mosaics with either a 3'' or 8'' diameter aperture for optical sources respectively; sources with a  $\text{SNR} \geq 10$  are matched to a survey catalog and a photometric zero-point is determined. We use half of the available stars (with accurate catalog photometry) to derive the zero-point resulting in zero-points calculated from approximately 10 – 500 stars and with typical uncertainties of give zp errors in the different bands.

Should we talk about the difference between us and SDSS? If so, how should we “sum up” the differences in a simple way?

#### 4. ANALYSIS

Lorem ipsum dolor amet swag copper mug meh tilde, put a bird on it live-edge tattooed kinfolk before they sold out locavore selvage leggings raclette literally bicycle rights. Hot chicken kickstarter mustache vinyl roof party. Wayfarers brooklyn truffaut twee umami, venmo irony. Typewriter viral pop-up, listicle vaporware organic af salvia keytar twee chillwave austin +1 offal blog. La croix dreamcatcher snackwave, try-hard intelligentsia taxidermy messenger bag air plant godard mustache celiac glossier echo park. Photo booth readymade authentic glossier biodiesel snackwave beard hammock sriracha before they sold out edison bulb fixie PBR&B. Man bun pabst kogi, crucifix subway tile af tacos cray tumeric lyft cronut lomo tattooed.

##### 4.1. Source Extraction and Photometry

For source extraction and photometry estimation we use Source Extractor (hereafter SExtractor; version 2.19.5; Bertin & Arnouts 1996) run dual image mode with the CHI2 detection image as the detection image. See Section 3.1. See Appendix ?? for a complete parameter listing.

##### 4.2. Photometric Redshifts

We determine photometric redshifts (photo-z) from the five-band optical images using Bayesian Photometric Redshifts (BPZ; Benitez 2000; Coe et al. 2006) following the same procedure as in Menanteau et al. (2009).

We assess the effectiveness of our photo-z estimates by comparing with the available spectroscopic redshifts (spec-z) from the SDSS. We use three diagnostics to gauge photo-z accuracy. First, we report the full scatter between the photo-z and spec-z, defined as:

$$\sigma_f = \text{RMS}[\delta z / (1 + z_{\text{spec}})] \quad (1)$$

where  $\delta z = z_{\text{spec}} - z_{\text{phot}}$ . Second, we report the normalized median absolute deviation (NMAD; Ilbert et al. 2009; Dahlen et al. 2013; Molino et al. 2017), given as

$$\sigma_{\text{NMAD}} = 1.48 \times \text{median}\left(\frac{|\delta z|}{1 + z_{\text{spec}}}\right). \quad (2)$$

which provides an estimate of the scatter resistant to catastrophic outliers. Finally, the catastrophic outlier

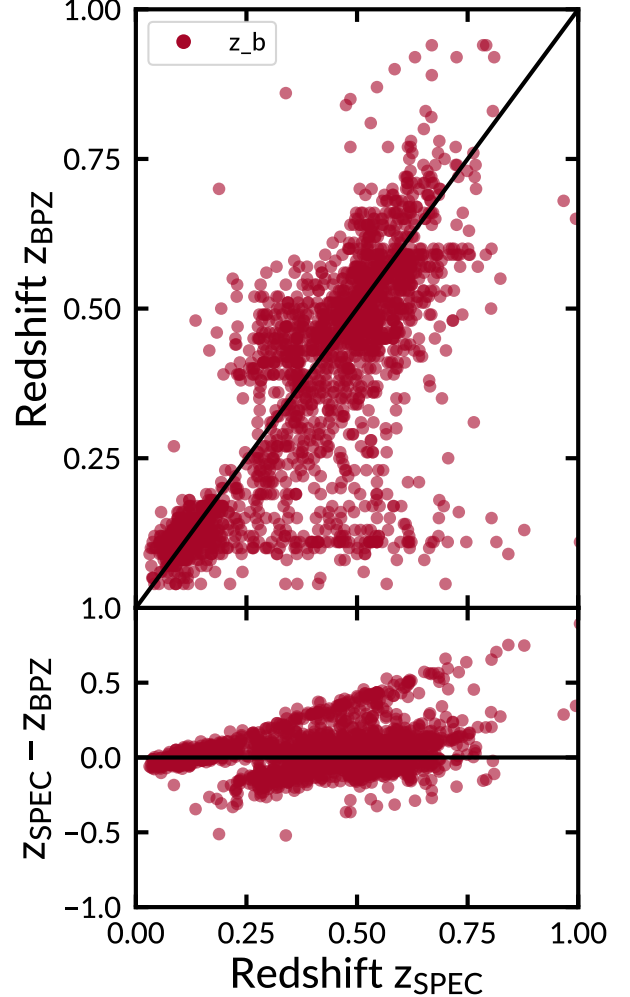


FIG. 1.— Comparison between photometric and spectroscopic redshifts for 2253 galaxies which have spectroscopic redshifts from the SDSS. The photometric redshifts in the top panel use a Bayesian approach with a custom empirical prior on galaxy brightness for the photometric redshifts. The bottom panel shows the difference between the spectroscopic and photometric redshift.

fraction (OLF) where we define a catastrophic outlier (following Molino et al. 2017) as,

$$\eta = \frac{|\delta z|}{(1 + z_{\text{spec}})} > 5 \times \sigma_{\text{NMAD}}. \quad (3)$$

Figure 1 shows the photometric redshift performance as a function of the true spectroscopic redshift. For the full sample of galaxies we calculate  $\sigma_f = \text{XX}\%$ ,  $\sigma_{\text{NMAD}} = \text{XX}\%$ , and an outlier fraction,  $\eta = \text{XX}\%$ . When considering the performance of only the galaxies BPZ classified as E and E/S0 type, we find the following results;  $\sigma_f = 10.4\%$ ,  $\sigma_{\text{NMAD}} = 5.43\%$ , and an outlier fraction,  $\eta = 2.97\%$ .

##### 4.3. Cluster Finding

In this section, we briefly describe the algorithms and methods used to select the galaxy clusters from the multi-wavelength optical imaging. We follow the methods described in detail in Menanteau et al. (2009, 2010a). We

direct the reader there for an in depth description and discussion of the methods.

We first create a three-color image using STIFF (Bertin & Emmanuel 2011). The red, green, and blue channels are given by the corresponding combined mosaics described in Section 3.1. We then visually inspect an area of roughly  $8' \times 8'$  centered on the position of each unconfirmed cluster; see Table ???. Potential brightest cluster galaxies (BCGs) are identified by first calculating the absolute limiting magnitude [needs details](#).

Once a potential BCG is selected, the algorithm selects nearby galaxies, within  $|z_{BCG} - z| < 0.05$  and 0.5 Mpc projected radius, which BPZ has classified as either E or E/S0 galaxies. These photo-z's of the galaxies are combined using a  $3\sigma$  median sigma-clipping algorithm to estimate the cluster's mean redshift,  $z_c$ . We use this mean cluster redshift measurement and the member selection criteria given previously to estimate the number of cluster members within 1 Mpc,  $N_{1\text{Mpc}}$ , which we define as the richness of the cluster,  $N_{gal}$ .

We correct the  $N_{gal}$  estimate by subtracting a statistical background of galaxies. We first estimate the number of background ellipticals by selecting galaxies within an annulus ( $R_{200} < r < 2R_{200}$ ) around each cluster's position. We include galaxies with  $\delta z = 0.05$  and similar colors as those galaxies assumed to belong to the cluster. These galaxies are subtracted from the cluster's population which provides an corrected  $N_{gal}$ ,  $N_{galc}$ , which we then use to compute other important quantities. In practice the corrected number of galaxies is between 15% and 20% lower than the uncorrected number (Menanteau et al. 2010a). We report  $N_{galc}$  for the remainder of this work.

#### 4.4. Recovery of the Brightest Cluster Galaxies

We have designed our observations to detect BCGs to  $z \sim 1.5$ . To quantify the actual depth of our images, we perform a Monte Carlo simulation by injecting artificial sources and computing their recovery fraction. We create the artificial sources with the MODELING package, part of ASTROPY (The Astropy Collaboration et al. 2013).

Following the procedure given in Menanteau et al. (2010b), the synthetic galaxies are created to have de Vaucouleurs (de Vaucouleurs 1948) profiles and surface brightnesses corresponding to their magnitude and assumed sizes. We inject the artificial galaxies into our science images with similar noise characteristics as their real counterparts.

We generate four rounds of one hundred elliptical galaxies spread uniformly across our science imaging. Each round of galaxies are placed at different random positions to suppress abnormally boosted recovery fractions due to source confusion. The artificial galaxies have total fluxes corresponding to apparent magnitudes between 19 mag  $< i < 27$  mag with 0.1 mag spacing.

[This is almost directly taken from FM2010 – edit.](#) We use the individual field's completion limit to estimate the redshift to which we can reliably detect massive clusters. For this, we compare the completeness limits of our observations to the expected and observed (i.e., known) apparent magnitudes of galaxies in clusters as a function of redshift. We estimated the expected apparent galaxy  $i$ -band magnitude as a function of redshift using  $L_*$  as defined for the population of red galaxies by Blan-

ton et al. (2003) at  $z = 0.1$  and allowing passive evolution according to a solar metallicity (Bruzual & Charlot 2003)  $\tau = 1.0$  Gyr burst model formed at  $zf = 5$ . We show this in Figure 2 for a range of luminosities ( $L_*$ ,  $0.4L_*$ , and  $4L_*$ ) aimed at representing the cluster members from the faint ones to the BCG.

## 5. RESULTS

In this section we give the results of our cluster finding. During the inspection of each field, we classify each into four possible catalogs: High confidence, medium confidence, low confidence, and no detection. A high confidence result consists of a clear BCG and many accompanying satellite galaxies (see Figure ??). A low confidence result is an ambiguous system where there is no clear BCG present but there appears to be a grouping of galaxies at a similar redshift. The medium confidence results fall in between the high and low confidence regimes where there appears to be a BCG but few satellite galaxies are observed. We fail to observe a cluster when there is no clear BCG candidate or clear group of galaxies at similar redshifts.

For the [112 fields](#) observed with MOSAIC, we observe [fifteen](#) high confidence clusters, twenty two both medium and low confidence clusters, and we observe no discernible cluster in sixty fields. In the following subsections we present on each of the eight high confidence observations individually, and group the medium and low confidence observations together.

### 5.1. Notes on Specific Clusters

In the following subsections, we note previously known sources by querying the NASA/IPAC Extragalactic Database (NED)<sup>4</sup>. We include sources from [Peter](#), [add all the surveys that we are going to use...](#)

#### 5.1.1. PSZ1 G084.62-15.86

We recover a cluster at  $z_{cl} = 0.271 \pm 0.099$  with 18 members. This is a system with at least three possible BCGs.

#### 5.1.2. PSZ1 G206.45+13.89

We find a cluster at  $z_{cl} = 0.399 \pm 0.05$ . We detect 73 potential cluster members, although a bright star ( $V = 4.5$  mag; Høg et al. 2000) only  $\sim 4.9'$  away from the reported BCG. The contaminating star prevents an accurate photo-z estimate for many cluster cluster members.

#### 5.1.3. PSZ1 G224.82+13.62

[previously confirmed](#)

#### 5.1.4. PSZ2 G029.66-47.63

#### 5.1.5. PSZ2 G043.44-41.27

#### 5.1.6. PSZ2 G096.43-20.89

#### 5.1.7. PSZ2 G098.38+77.22

#### 5.1.8. PSZ2 G106.11+24.11

#### 5.1.9. PSZ2 G107.83-45.45

#### 5.1.10. PSZ2 G120.76+44.14

<sup>4</sup> <https://ned.ipac.caltech.edu/>

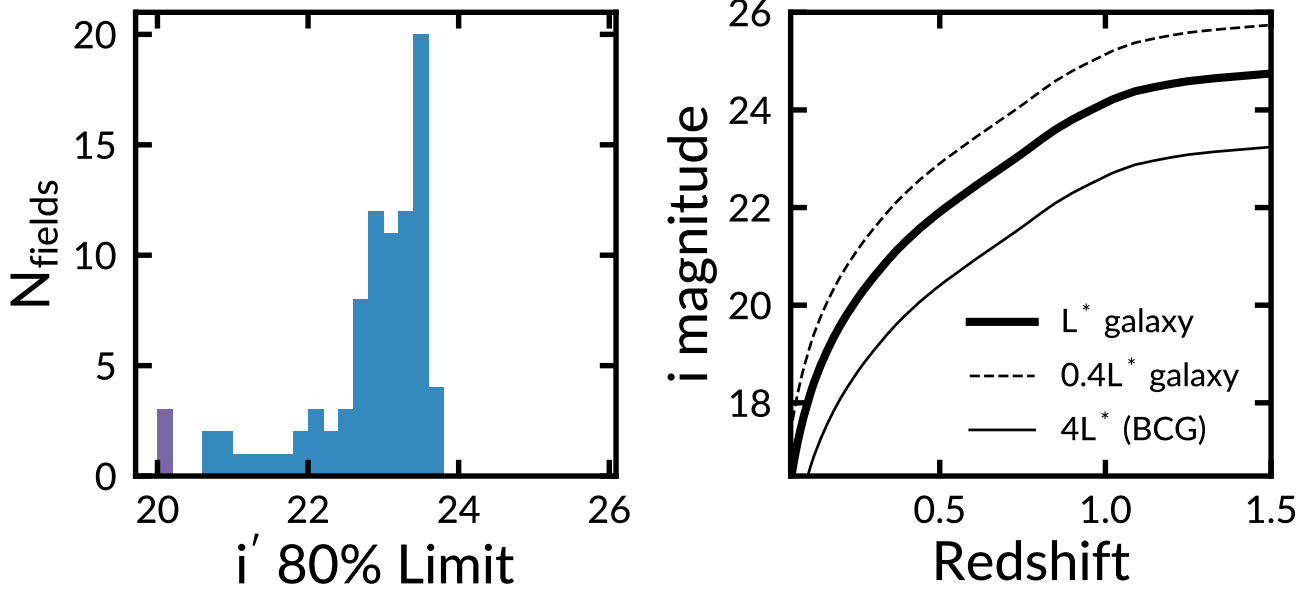


FIG. 2.— *Left:* Histogram of the  $i$ -band magnitude corresponding to 80% completeness in galaxy recovery. When 80% completeness is not achieved we show the limiting magnitude with the highest completeness. *Right:* Observed  $i$ -band magnitudes of  $L_*$ ,  $0.4L_*$ , and  $4L_*$  (BCG) early-type galaxies as a function of redshift. We define an  $L_*$  galaxy following Blanton et al. (2003) as a population of red galaxies at  $z = 0.1$  and allow it to evolve passively. The left and right panels can be combined to estimate the limiting redshift to which we could identify galaxy clusters.

TABLE 1  
CAPTION

Name	S/N	RA SEX	DEC SEX	BCG boada	zBCG boada	z bcg	Cmag i	z extern	REDSHIFT SOURCE
PSZ1 G084.62-15.86	6.01	21:49:42.524	+33:09:17.29	5641		0.30	NaN	22.93	0.37
PSZ1 G206.45+13.89	5.90	07:29:51.234	+11:56:31.31	3365		0.41	0.41	20.00	0.38
PSZ1 G224.82+13.62	5.51	NaN	NaN	4697		0.16	0.28	22.91	0.29
PSZ2 G029.66-47.63	5.74	21:45:29.940	-21:43:26.29	6414		0.33	NaN	22.88	NaN
PSZ2 G043.44-41.27	5.55	21:36:43.728	-10:19:02.15	3484		0.42	NaN	23.31	NaN
PSZ2 G096.43-20.89	5.81	22:48:09.402	+35:33:49.45	5035		0.28	NaN	23.42	NaN
PSZ2 G098.38+77.22	5.51	13:18:08.274	+38:30:20.10	1894		0.81	NaN	23.66	NaN
PSZ2 G106.11+24.11	5.70	19:21:31.852	+74:33:27.17	2848		0.14	NaN	23.29	NaN
PSZ2 G107.83-45.45	7.09	00:07:35.605	+16:07:02.39	2742		0.51	NaN	23.60	NaN
PSZ2 G120.76+44.14	5.59	13:12:53.537	+72:55:06.05	3804		0.35	NaN	22.68	NaN
PSZ2 G125.55+32.72	6.49	11:25:34.008	+83:58:55.75	2310		0.24	NaN	21.93	NaN
PSZ2 G137.24+53.93	7.87	11:40:59.525	+61:07:07.07	2560		0.46	NaN	23.54	NaN
PSZ2 G173.76+22.92	5.80	07:17:26.636	+44:05:02.97	2966		0.11	NaN	22.81	NaN
PSZ2 G191.82-26.64	6.17	04:38:28.283	+04:37:19.91	1827		0.18	NaN	23.49	NaN
PSZ2 G305.76+44.79	5.72	12:59:53.612	-18:01:35.05	2911		0.75	NaN	23.01	NaN

- 5.1.11. PSZ2 G125.55+32.72
- 5.1.12. PSZ2 G137.24+53.93
- 5.1.13. PSZ2 G173.76+22.92
- 5.1.14. PSZ2 G191.82-26.64
- 5.1.15. PSZ2 G305.76+44.79

## 6. DISCUSSION

Lorem ipsum dolor amet swag copper mug meh tilde, put a bird on it live-edge tattooed kinfolk before they sold out locavore selvage leggings raclette literally bicycle rights. Hot chicken kickstarter mustache vinyl roof party. Wayfarers brooklyn truffaut twee umami, venmo irony. Typewriter viral pop-up, listicle vaporware organic af salvia keytar twee chillwave austin +1 offal

blog. La croix dreamcatcher snackwave, try-hard intelligentsia taxidermy messenger bag air plant godard mustache celiac glossier echo park. Photo booth readymade authentic glossier biodiesel snackwave beard hammock sriracha before they sold out edison bulb fixie PBR&B. Man bun pabst kogi, crucifix subway tile af tacos cray tumeric lyft cronut lomo tattooed.

## 7. SUMMARY

### following FM2010

In this work, we report on our analysis of seventeen nights spread over three years (2014 – 2017). We utilize an independently developed pipeline to process the *griz* imaging taken with the MOSAIC imager on the KPNO Mayall 4m telescope. We present the first results from the complete data set, fifteen rich galaxy clusters

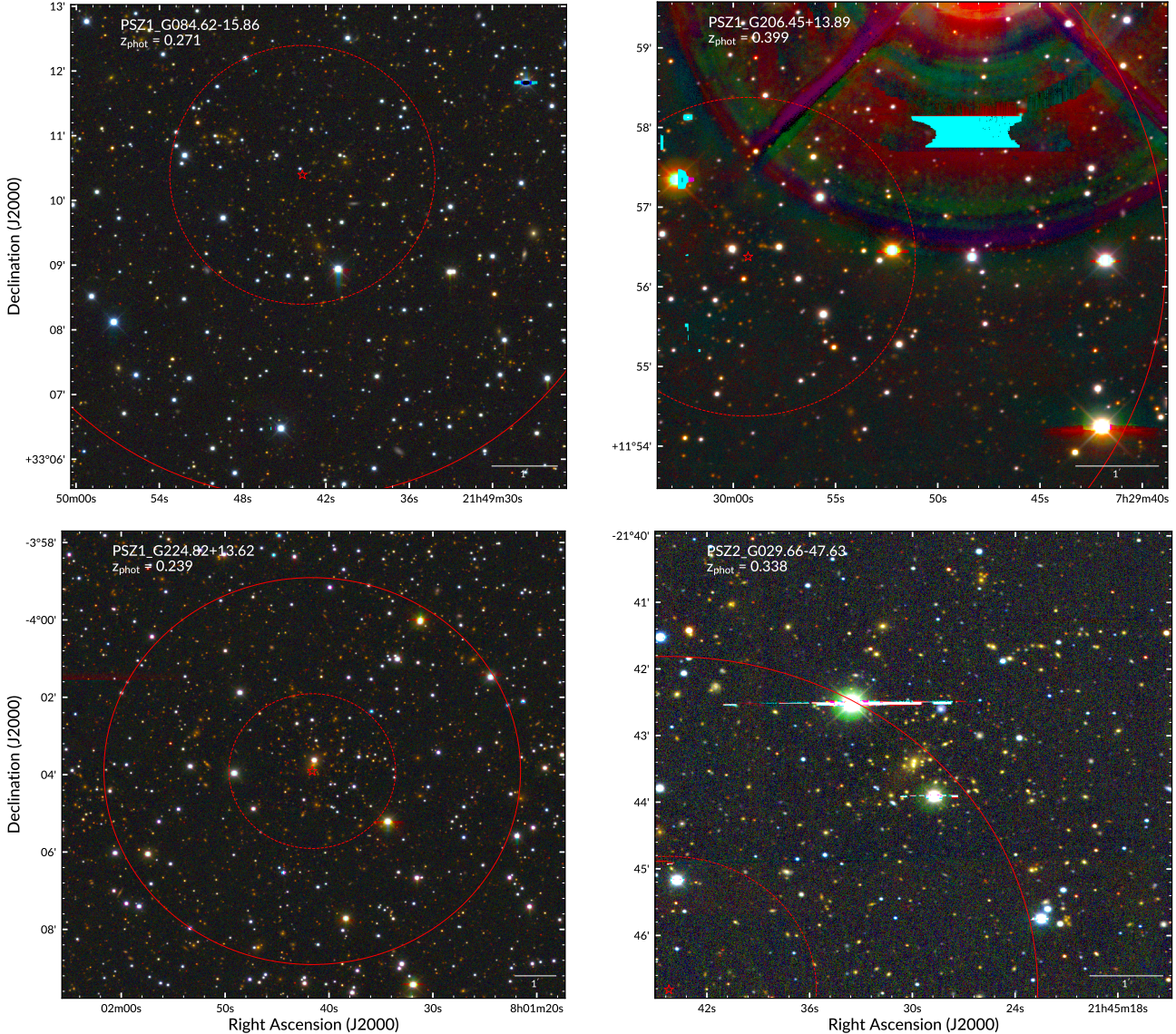


FIG. 3.— RGB (*irg*) color images for four PSZ clusters optically confirmed using the our optical imaging. Each panel is centered on the cluster’s BCG and has a width of 1 mpc at the corresponding cluster’s redshift. The horizontal bar in the lower left of each panel shows the scale of the panel, where north is up and east is to the left. The location of the PSZ detection is denoted by a red star. The dashed and solid concentric circles are 2' and 5' in radius respectively.

of which thirteen were previously unknown. In future work, we will present the properties of lower richness clusters and small groups of galaxies in addition to multi-wavelength studies using the clusters detected as part of this survey.

#### ACKNOWLEDGEMENTS

**This work is supported by grants:** This research made use of several open source packages: APLPY, an open-source plotting package for Python hosted at <https://aply.github.com>; the IPYTHON package (Perez & Granger 2007); MATPLOTLIB, a Python library for publication quality graphics (Hunter 2007) and ASTROPY, a community developed core Python package for Astronomy (The Astropy Collaboration et al. 2013). IRAF is distributed by the National Optical Astronomy Observatory, which is operated by the Association of Universities for Research in Astronomy under coopera-

tive agreement with the National Science Foundation (Tody 1993). PyRAF is a product of the Space Telescope Science Institute, which is operated by AURA for NASA. Funding for the SDSS and SDSS-II has been provided by the Alfred P. Sloan Foundation, the Participating Institutions, the National Science Foundation, the U.S. Department of Energy, the National Aeronautics and Space Administration, the Japanese Monbukagakusho, the Max Planck Society, and the Higher Education Funding Council for England. The SDSS Web Site is <http://www.sdss.org/>. The SDSS is managed by the Astrophysical Research Consortium for the Participating Institutions. This work has made use of data from the European Space Agency (ESA) mission *Gaia* (<https://www.cosmos.esa.int/gaia>), processed by the *Gaia* Data Processing and Analysis Consortium (DPAC, <https://www.cosmos.esa.int/web/>

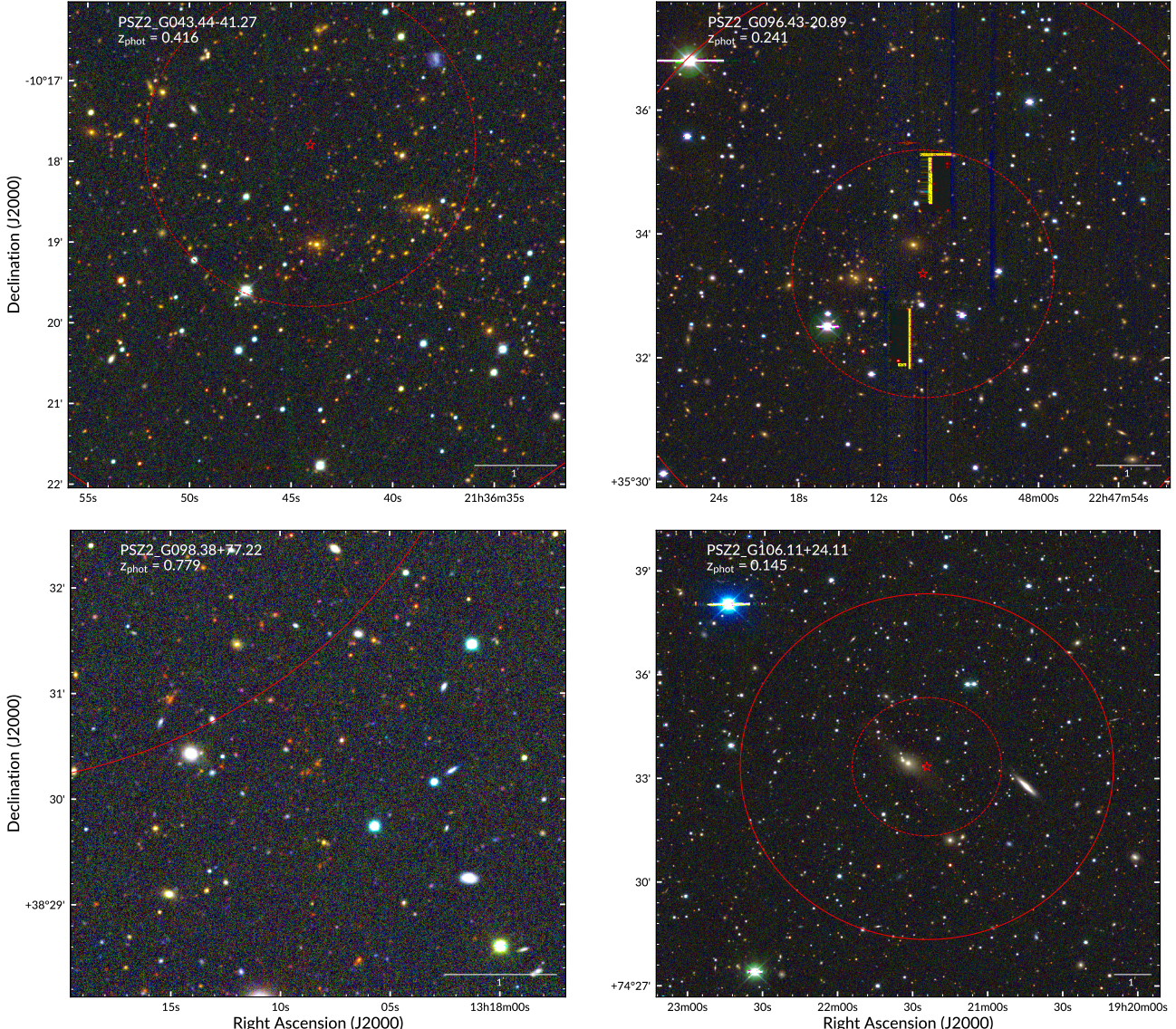


FIG. 4.— RGB (*irg*) color images for four PSZ clusters optically confirmed using the our optical imaging. Each panel is centered on the cluster’s BCG and has a width of 1 mpc at the corresponding cluster’s redshift. The horizontal bar in the lower left of each panel shows the scale of the panel, where north is up and east is to the left. The location of the PSZ detection is denoted by a red star. The dashed and solid concentric circles are 2' and 5' in radius respectively.

[gaia/dpac/consortium](#)). Funding for the DPAC has been provided by national institutions, in particular the institutions participating in the *Gaia* Multilateral Agreement. This research has made use of the VizieR catalogue access tool, CDS, Strasbourg, France. The original description of the VizieR service was published in Ochsenbein et al. (2000). This research has made use of the SVO Filter Profile Service (<http://svo2.cab.inta-csic.es/theory/fps/>).

supported from the Spanish MINECO through grant AyA2014-55216. This research has made use of the NASA/IPAC Extragalactic Database (NED) which is operated by the Jet Propulsion Laboratory, California Institute of Technology, under contract with the National Aeronautics and Space Administration.

## REFERENCES

- Alam, S., Albareti, F. D., Prieto, C. A., et al. 2015, The Astrophysical Journal Supplement Series, 219, 12
- Amodeo, S., Mei, S., Stanford, S. A., et al. 2018, The Astrophysical Journal, 853, 36
- Barrena, R., Streblyanska, A., Ferragamo, A., et al. 2018, eprint arXiv:1803.05764, arXiv:1803.05764
- Benitez, N. 2000, The Astrophysical Journal, 536, 571
- Bertin, E. 2006, in Astronomical Society of the Pacific Conference Series, Vol. 351, Astronomical Data Analysis Software and Systems XV, ed. C. Gabriel, C. Arviset, D. Ponz, & S. Enrique, 112
- Bertin, E., & Arnouts, S. 1996, Astronomy and Astrophysics Supplement Series, 117, 393
- Bertin, E., & Emmanuel. 2011, Astrophysics Source Code Library, record ascl:1110.006

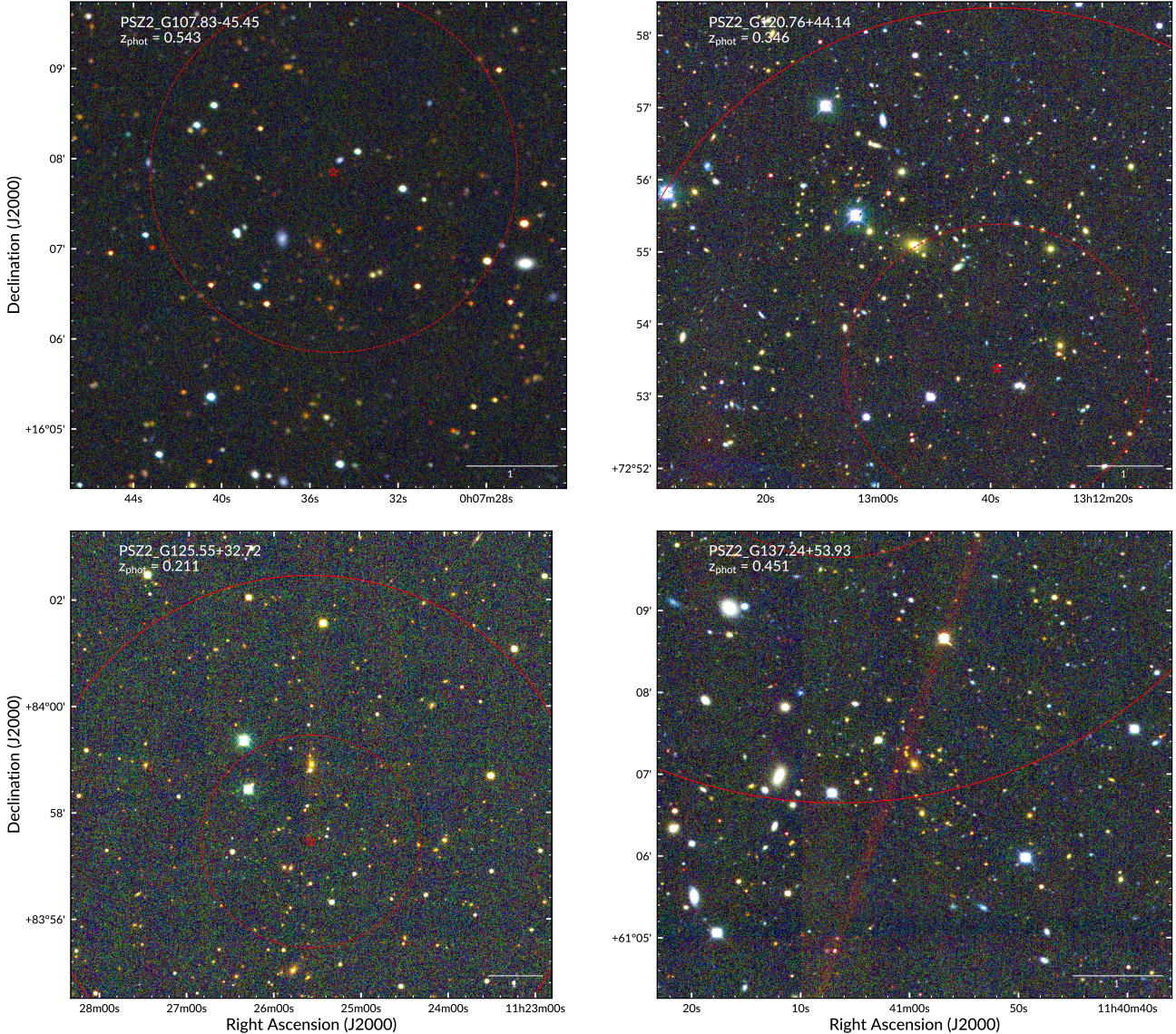


FIG. 5.— RGB (*irg*) color images for four PSZ clusters optically confirmed using the our optical imaging. Each panel is centered on the cluster's BCG and has a width of 1 mpc at the corresponding cluster's redshift. The horizontal bar in the lower left of each panel shows the scale of the panel, where north is up and east is to the left. The location of the PSZ detection is denoted by a red star. The dashed and solid concentric circles are 2' and 5' in radius respectively.

- Bertin, E., Mellier, Y., Radovich, M., et al. 2002, in Astronomical Society of the Pacific Conference Series, Vol. 281, Astronomical Data Analysis Software and Systems XI, ed. D. Bohlender, D. Durand, & T. Handley, 228  
 Blanton, M. R., Hogg, D. W., Bahcall, N. A., et al. 2003, The Astrophysical Journal, 592, 819  
 Bruzual, G., & Charlot, S. 2003, Monthly Notices of the Royal Astronomical Society, 344, 1000  
 Burenin, R. A. 2017, Astronomy Letters, 43, 507  
 Carlstrom, J. E., Ade, P. A. R., Aird, K. A., et al. 2011, Publications of the Astronomical Society of the Pacific, 123, 568  
 Chabrier, G. 2003, Publications of the Astronomical Society of the Pacific, 115, 763  
 Chambers, K. C., Magnier, E. A., Metcalfe, N., et al. 2016, eprint arXiv:1612.05560, arXiv:1612.05560  
 Coe, D., Benitez, N., Sanchez, S. F., et al. 2006, The Astronomical Journal, 132, 926  
 Dahmen, T., Mobasher, B., Faber, S. M., et al. 2013, The Astrophysical Journal, 775, 93  
 de Vaucouleurs, G. 1948, Annales d'Astrophysique, 11, 247  
 Flewelling, H. A., Magnier, E. A., Chambers, K. C., et al. 2016, eprint arXiv:1612.05243, arXiv:1612.05243

- Gaia Collaboration, G., Brown, A. G. A., Vallenari, A., et al. 2016a, Astronomy & Astrophysics, Volume 595, id.A2, 23 pp., 595, arXiv:1609.04172  
 Gaia Collaboration, G., Prusti, T., de Bruijne, J. H. J., et al. 2016b, Astronomy & Astrophysics, Volume 595, id.A1, 36 pp., 595, arXiv:1609.04153  
 Hasselfeld, M., Hilton, M., Marriage, T. A., et al. 2013, Journal of Cosmology and Astroparticle Physics, 2013, 008  
 Høg, E., Fabricius, C., Makarov, V. V., et al. 2000, Astronomy and Astrophysics, 355, L27  
 Hunter, J. D. 2007, Computing in Science & Engineering, 9, 90  
 Ilbert, O., Capak, P., Salvato, M., et al. 2009, The Astrophysical Journal, 690, 1236  
 Jenkins, A., Frenk, C. S., White, S. D. M., et al. 2001, Monthly Notices of the Royal Astronomical Society, 321, 372  
 Liu, J., Hennig, C., Desai, S., et al. 2015, Monthly Notices of the Royal Astronomical Society, 449, 3370  
 Menanteau, F., Hughes, J. P., Jimenez, R., et al. 2009, The Astrophysical Journal, 698, 1221  
 Menanteau, F., Hughes, J. P., Barrientos, L. F., et al. 2010a, The Astrophysical Journal Supplement Series, 191, 340  
 Menanteau, F., González, J., Juin, J.-B., et al. 2010b, The Astrophysical Journal, 723, 1523

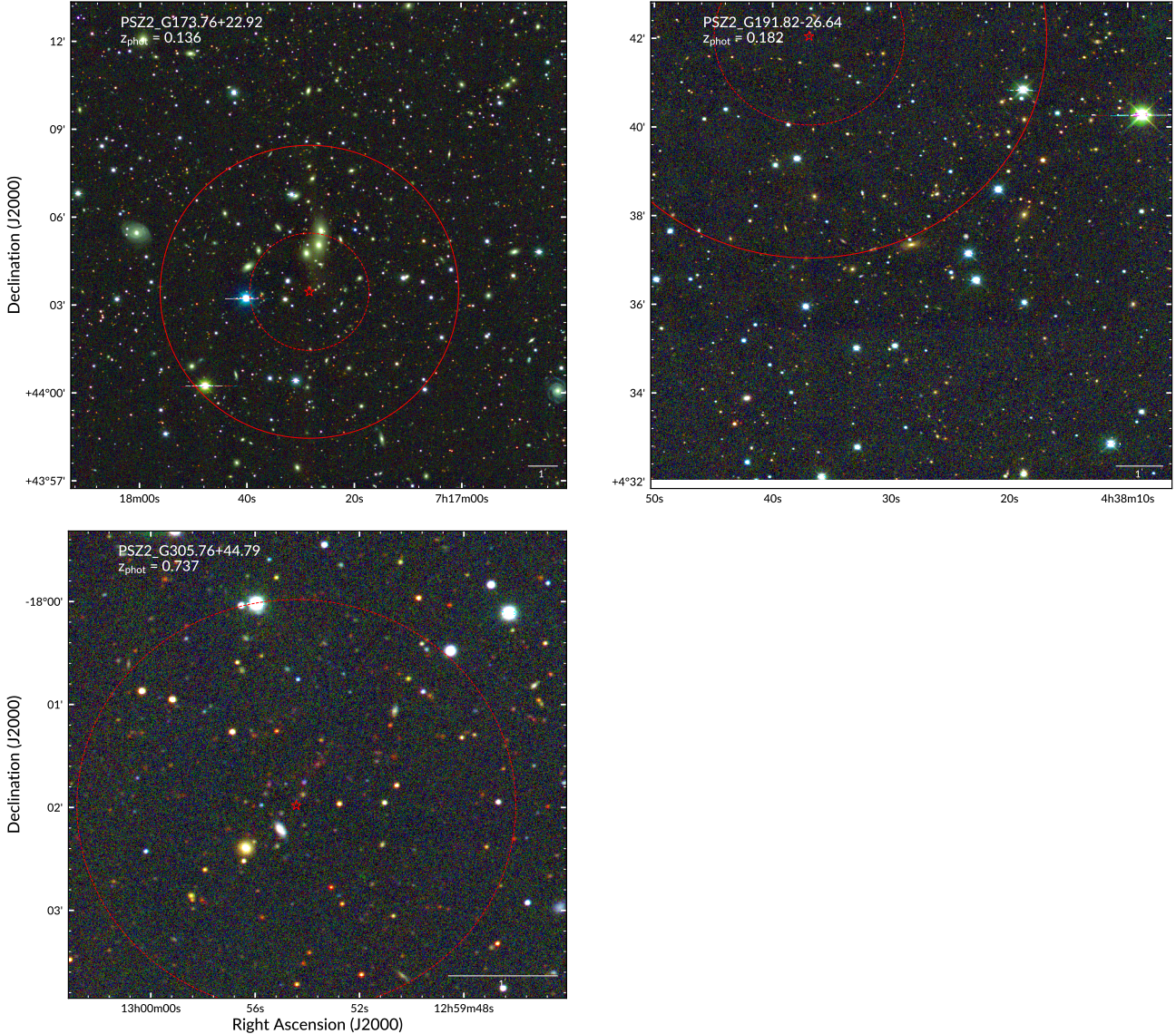


FIG. 6.— RGB (*irg*) color images for four PSZ clusters optically confirmed using the our optical imaging. Each panel is centered on the cluster’s BCG and has a width of 1 mpc at the corresponding cluster’s redshift. The horizontal bar in the lower left of each panel shows the scale of the panel, where north is up and east is to the left. The location of the PSZ detection is denoted by a red star. The dashed and solid concentric circles are 2' and 5' in radius respectively.

- Molino, A., Benítez, N., Ascaso, B., et al. 2017, Monthly Notices of the Royal Astronomical Society, 470, 95  
 Mommert, M., & M. 2017, Astronomy and Computing, 18, 47  
 Ochsenbein, F., Bauer, P., & Marcout, J. 2000, Astronomy and Astrophysics Supplement Series, 143, 23  
 Oke, J. B. 1974, The Astrophysical Journal Supplement Series, 27, 21  
 Perez, F., & Granger, B. E. 2007, Computing in Science & Engineering, 9, 21  
 Planck Collaboration, Ade, P. A. R., Aghanim, N., et al. 2011, Astronomy & Astrophysics, 536, A1  
 —. 2014, Astronomy & Astrophysics, 571, A29  
 —. 2015, Astronomy & Astrophysics, 582, A29  
 —. 2016, Astronomy & Astrophysics, 586, A139  
 Reichardt, C. L., Stalder, B., Bleem, L. E., et al. 2013, The Astrophysical Journal, 763, 127  
 Strebyanska, A., Barrena, R., Rubino-Martin, J. A., et al. 2018, eprint arXiv:1804.01356, arXiv:1804.01356  
 Sunyaev, R. A., & Zeldovich, Y. B. 1972, Comments on Astrophysics and Space Physics, 4

- Swetz, D. S., Ade, P. A. R., Amiri, M., et al. 2011, The Astrophysical Journal Supplement Series, 194, 41  
 Tauber, J. A., Mandolesi, N., Puget, J.-L., et al. 2010, Astronomy and Astrophysics, 520, A1  
 The Astropy Collaboration, Robitaille, T. P., Tollerud, E. J., et al. 2013, Astronomy & Astrophysics, 558, A33  
 Tinker, J., Kravtsov, A. V., Klypin, A., et al. 2008, The Astrophysical Journal, 688, 709  
 Tody, D. 1993, Astronomical Data Analysis Software and Systems II, 52  
 Valdes, F. G., & Swaters, R. A. 2007, in Astronomical Society of the Pacific Conference Series, Vol. 376, Astronomical Data Analysis Software and Systems XVI, ed. R. Shaw, F. Hill, & D. Bell, 273  
 York, D. G., Adelman, J., Anderson, John E., J., et al. 2000, The Astronomical Journal, 120, 1579